Bifunctional integration of La-Ni diatomic sites with optical and catalytical activity for efficient CO2 photoreduction

Min Zhou
   Wuhan University of Technology

Zhiqing Wang
   Wuhan University of Technology

Aohan Mei
   Wuhan University of Technology

Zifan Yang
   Wuhan University of Technology

Wen Chen
   School of Materials Science and Engineering

Siyong Ou
   Wuhan University of Technology

Kun Qi
   Institut Européen des Membranes   https://orcid.org/0000-0002-5574-4475

Jingyuan Ma
   Shanghai Advanced Research Institute, Chinese Academy of Sciences

Shengyao Wang
   Huazhong Agricultural University   https://orcid.org/0000-0002-2748-483X

Keqiang Chen (✉ chenkeqiang@cug.edu.cn)
   Wuhan University of Technology   https://orcid.org/0000-0002-5741-1236

Peter Reiss
   Grenoble Alpes University   https://orcid.org/0000-0002-9563-238X

Yueli Liu
   State Key Laboratory of Silicate Materials for Architectures, School of Materials Science and Engineering, Wuhan University of Technology, Wuhan, 430070, P. R. China   https://orcid.org/0000-0001-5960-8166

Article

Keywords: Covalent organic frameworks, Photocatalysis, CO2 reduction, Dual-atom catalyst, Synergistic effect

Abstract

Dual-atom catalysts possess a significant potential for promoting CO_2 photoreduction to lucrative solar fuels. However, the precise construction of the diatomic sites that simultaneously foster light absorption and catalytic activity is a formidable challenge, as both processes follow distinct pathways in the photocatalyst. Herein, a facile electrostatic-driven self-assembling approach is employed to realize a bifunctional architecture of a diatomic LaNi-Phen (Phenanthroline)/covalent organic framework (COF-5) photocatalyst. The La site acts as an optically active center for the photoinduced generation of carriers, while the Ni site serves as the catalytically active center for highly selective CO_2-to-CO reduction enabled by directional charge transfer via COF-5. Density functional theory (DFT) calculations and in-situ characterization reveal the efficient synergistic effect of the La-Ni double-atomic sites, leading to decreased reaction energy barriers of *COOH intermediate and enhanced CO_2-to-CO conversion. As a result, in the absence of any additional photosensitizers, a 15.2 times enhancement of the CO_2 reduction rate (605.8 $\mu mol \cdot g^{-1} \cdot h^{-1}$) over that of pristine COF-5 colloid (39.9 $\mu mol \cdot g^{-1} \cdot h^{-1}$) and an improvement in CO selectivity to 98.2% are achieved. This work presents a novel strategy for integrating optically and catalytically active centers, which results in a diatomic synergy effect enabling high-performance photocatalytic CO_2 reduction.

Introduction

Artificial solar-driven CO_2 reduction to renewable fuels (e.g., CO[1], HCOOH[2], HCHO[3], CH_3OH[4], and CH_4[5,6]) based on semiconductor-mediated photocatalysis is an intriguing strategy for producing carbon-neutral energy, while also mitigating emerging environmental crises[7,8]. Developing effective photocatalysts with high activity and selectivity has become one of the foremost challenges towards accomplishing this objective[9]. Atomically dispersed catalysts exhibiting maximum atom utilization and unrivaled photoelectric performance are considered the most promising candidates[10-11]. Recently, single-atom catalysts (SACs) with atomically distributed catalytic metal sites have demonstrated impressive catalytic performance in the selective CO_2 reduction reaction (CO_2RR)[12-14]. However, their limited light absorption capacity and production of numerous intermediates and by-products impede their further implementation. Moreover, the catalytic activity of SACs is limited by the lack of synergistic active sites, inadequate suppression of the competing hydrogen evolution reaction (HER), and weak interaction with the substrate materials[15-17].

Generally, the CO_2RR entails three primary processes: photoabsorption, carrier separation, and CO_2 reduction[18-21]. Therefore, ideal photocatalysts should possess a sufficient optically active center to generate photoinduced charges as well as an efficient channel to transfer these carriers to a catalytically active center of high selectivity. In contrast to SACs with single catalytic sites, dual-atom catalysts (DACs) with bimetallic centers exhibit tremendous potential for the combination of atom-specific characteristics due to the synergistic effect and more complex functionalities between adjacent active sites[22,23]. The

latter can lead to the enhanced generation of photoinduced charges and improved catalytic activity while maintaining high atom utilization, stability, and properties, which are constrained by the nature of the atomic dispersion[24–29]. As an example, the synergistic effect of two sets of single-atom sites (Ni and Fe) anchored on nitrogenated carbon has recently been demonstrated to yield an efficient electrocatalyst for the CO_2RR, which significantly reduced the reaction barriers for the formation of COOH* and desorption of CO, and resulted in a structural evolution into the CO-adsorbed moiety upon CO_2 uptake[30]. Therefore, rationally developed bimetallic site photocatalysts can be used to effectively modulate the selectivity and activity of the CO_2RR by controlling the reaction pathway[31]. However, substantial challenges persist in acquiring a comprehensive understanding of the precise roles of the specific single-atom sites and the synergistic mechanisms occurring at the atomic level during the dynamic photocatalytic CO_2RR process.

Among possible scaffolds for the integration of the dual-atomic sites, crystalline porous network materials such as metal-organic frameworks (MOFs) and covalent organic frameworks (COFs) are renowned for their well-defined porosity, high specific surface area, and predetermined structure[32–36]. These features combined with the confining influence of the ordered pore structure and the abundance of surface binding groups produce a highly favorable environment for the anchoring of metal atoms[37–41]. On the other hand, there are only a few scarce in-depth studies elucidating the critical role of the substrates in the CO_2RR process. From the perspective of DACs, a strong interaction between the catalyst and the substrate is desired to improve the catalytic stability. Furthermore, the interaction between the catalyst and the substrate modulates the processes of carrier separation and transfer and thus has a direct influence on the catalytic performance.

In this paper, we develop an electrostatically driven self-assembling strategy for incorporating atomically dispersed La-Ni sites (specifically, LaNi-Phen, where Phen = phenanthroline) into conjugated boronate-ester-linked COFs (COF-5 colloid, supplementary Fig. 1). This novel La-Ni coordination structure is designed to enable efficient production and transfer of photoinduced charges through the optically active (La site) and catalytically active (Ni site) centers. We demonstrate the synergistic action of the La and Ni sites and unravel the role of the substrate, fostering the effective transfer of the photogenerated carriers. As a result, the optimized LaNi-Phen/COF-5 photocatalyst without any additional photosensitizer exhibits a CO evolution activity of 605.8 $\mu mol \cdot g^{-1} h^{-1}$ with high selectivity (98.2%), corresponding to a remarkable 15.2-times activity improvement over pristine COF-5 colloid. Experimental characterization data and theoretical calculations confirm that the COF-5 colloid operates as an electron transfer channel through interactions with electrostatically self-assembled La-Phen and Ni-Phen in a mechanism that comprises photoelectron transfer from La-Phen to the COF-5 colloid and subsequent electron injection into Ni-Phen for the CO_2RR process. This work provides a novel, scalable strategy for producing ligand-assisted bimetallic self-assembled COF structures for efficient photocatalytic CO_2 reduction.

Results

Morphological and structural characterization. La-Ni bimetallic sites are incorporated into COF-5 colloid through a facile electrostatic-driven self-assembling process, in which the La and Ni atoms are captured by B atoms in COF-5 colloid and chelated by the Phen ligands (Fig. 1a), potentially facilitating CO_2RR (Fig. 1b). Powder X-ray diffraction (PXRD) patterns demonstrate that the crystalline structure of COF-5 colloid remains unaltered throughout the self-assembly process (Supplementary Fig. 2)[42]. The morphology of COF-5, as illustrated in Supplementary Figs. 3 and 4 displays a one-dimensional (1D) nanorods structure with a width of 70–80 nm. Further studies indicate that there is no discernible presence of discrete La-Ni nanoparticles in as-synthesized LaNi-Phen/COF-5 (Fig. 2a), but that the La and Ni ions are uniformly dispersed throughout the COF-5 colloid, with no sign of segregation or aggregation (Fig. 2b). Importantly, as illustrated in Fig. 2c, the atomically dispersed La and Ni ions in COF-5 colloid are visible using aberration-corrected high-angle annular dark-field scanning transmission electron microscopy (AC-HAADF-STEM). X-ray photoelectron spectroscopy (XPS) results reveal that the valence states of the Ni and La ions are + 2 and + 3, respectively (Supplementary Fig. 6, and Supplementary Note 1). In addition, the strong coordination of nitrogen atoms in Phen with Ni and La ions is confirmed by the energetic upshift of the N 1s peaks (Supplementary Fig. 7). The formation of metal-nitrogen bonds is further corroborated by the slight bathochromic shift of the FTIR bands, as depicted in Supplementary Fig. 8 and Supplementary Note 2. The specific elemental contents of La and Ni in LaNi-Phen/COF-5 are calculated to be 2.58 and 1.61 wt%, respectively (Supplementary Fig. 9 and Supplementary Table 1). Notably, the COF-5 colloid in LaNi-Phen/COF-5 comprises a high specific surface area, open pore structure, and outstanding CO_2 capture capability, ensuring good access to the La-Ni active sites by CO_2 molecules in the photocatalytic process (Supplementary Fig. 10–13 and Supplementary Note 3). Moreover, when compared to the host COF-5 colloids, the UV-vis absorption spectrum of LaNi-Phen/COF-5 exhibits a red-shift indicative of a more favorable energy level alignment for CO_2 reduction (Supplementary Fig. 14–16 and Supplementary Note 4). When comparing to Ni-Phen/COF-5, the modification of COF-5 colloid with La ions alone already leads to a significant red-shift of the absorption onset, implying that the introduction of the rare earth metal La as the optically active center results in enhanced light-harvesting properties and a high degree of electron delocalization in COF-5 colloid.

The atomic structure and coordination environment of LaNi-Phen/COF-5 are explored further using X-ray absorption fine structure (XAFS) analysis. The X-ray absorption near-edge structure (XANES) spectrum is recorded to confirm the positive charge of La-Ni species due to their near-edge shoulder positioned between metal foils and metal oxides (Supplementary Fig. 17a-b). This is presumably attributed to the strong chelation effect of Phen and close interaction with COF-5 colloid. Furthermore, the dominant Ni-N and La-N peaks in the Fourier transform (FT) extended X-ray absorption fine structure (EXAFS) spectra of LaNi-Phen/COF-5 are near 1.57 and 1.72 Å, respectively (Fig. 2d, 2e), with no emergence of the characteristic peak of Ni-Ni (≈ 2.15 Å) and La-La bonding (≈ 3.94 Å). In other words, the atomic dispersion of La and Ni sites, as well as the absence of metal nanoparticles or clusters in LaNi-Phen/COF-5, are fully confirmed. Consistently, infrared (IR) spectroscopy analysis of the adsorbed CO on La-Phen/COF-5, Ni-Phen/COF-5, and LaNi-Phen/COF-5 reveals a set of CO absorption bands at 2117 cm^{-1}, which should be assigned to the characteristic frequency for the C-O stretching of the linearly adsorbed

CO on La-Ni ionic species (Fig. 2f). Furthermore, no obvious IR peak at 2092 cm^{-1} corresponding to La-Ni nanoparticles can be observed, confirming the absence of metal nanoparticles or clusters on LaNi-Phen/COF-5 catalysts, which further validates the AC-HAADF-STEM results (Fig. 2c). To reinforce these results, wavelet transform (WT) analysis is performed to discriminate different atoms within one atomic shell by resolving backscattering wave function centers in energy space. When compared with metal foil and metal oxides, the WT plots of LaNi-Phen/COF-5 exhibit only one maximum intensity at ca. 4.0 Å^{-1} (Ni K-edge) and 7.0 Å^{-1} (La L3-edge), which are primarily attributed to Ni-N and La-N contributions, indicating that La-Ni ions in LaNi-Phen/COF-5 exist as isolated single atoms without the presence of metallic crystalline species (Figs. 2g, 2h). La-N and Ni-N scattering at the first shell over LaNi-Phen/COF-5 with coordinated structures of La-N$_4$ and Ni-N$_2$ are further confirmed by the EXAFS fitting analyses (Fig. 2i, Supplementary Fig. 18–20, and Supplementary Table 2), which is consistent with the results of DFT optimization (Supplementary Fig. 21). Free LaNi-Phen was assembled to demonstrate the involvement of the pore confinement effect of COF-5 colloids in facilitating the formation of the La-N$_4$/Ni-N$_2$ coordination structure. The experimental results revealed that the bimetallic La-Ni center eventually self-assembles into a six-coordination structure (La-N$_6$/Ni-N$_6$) in the absence of COF-5 colloid, leading to undesired synergies because they are fully coordinated in the free state (Supplementary Fig. S21 and Supplementary Table 2). This result implies that the pore structure of COFs can significantly promote the precise modulation of the La-Ni diatomic structure, which is at the origin of the synergistic effect of LaNi-Phen in COF-5 colloids.

CO$_2$ photoreduction activity of LaNi-Phen/COF-5 catalysts. The CO$_2$ reduction reaction is conducted and described in the Methods section to evaluate the catalytic activity of LaNi-Phen/COF-5 under simulated solar irradiation. The CO$_2$RR performance of LaNi-Phen/COF-5 with various La-Ni metal proportions is monitored and optimized systematically (Supplementary Table 3), yielding the highest catalytic activity of 608 μmol·g^{-1}·h^{-1} (CO) and selectivity of 98.2% (CO over H$_2$). Significantly, the catalytic activity of the COF-5 colloid (39.9 μmol·g^{-1}·h^{-1}), La-Phen/COF-5 (195.4 μmol·g^{-1}·h^{-1}), and Ni-Phen/COF-5 (224.4 μmol·g^{-1}·h^{-1}) is 15.2, 3.1, and 2.7 times lower, respectively (Fig. 3a and 3b). Moreover, the CO selectivity is substantially higher than that of COF-5 colloid (70.7%), La-Phen/COF-5 (95.9%), and Ni-Phen/COF-5 (91.2%). We also investigated the CO$_2$RR performance of a physical mixture of La-Phen/COF-5 and Ni-Phen/COF-5 (denoted as mix-LaNi-Phen/COF-5), which exhibits significantly lower catalytic activity with a CO production rate of 115.9 μmol·g^{-1}·h^{-1}. These results unambiguously demonstrate the strong synergistic effect of the self-assembled La-Ni diatomic sites. Remarkably, the aforementioned activity and selectivity of LaNi-Phen/COF-5 are significantly higher than those of previously reported photocatalysts without unstable noble metal photosensitizers (Supplementary Table 4). Additionally, LaNi-Phen/COF-5 exhibits a higher total electron transfer (1,235.0 μmol g^{-1} h^{-1}) than other catalysts (Supplementary Table 5). As will be shown in the following, the outstanding CO$_2$RR performance in this work can be attributed to COF-5's intrinsic structural and electronic characteristics, as well as the synergistic effect of the self-assembled La-Ni diatomic sites. The foregoing results highlight the crucial role of COF-5 colloid and LaNi-Phen for achieving high performance, and control experiments conclusively confirm that it is an authentic CO$_2$RR process driven by continuous photoexcitation, in which

BIH and H_2O operate as electron sacrificial agents and proton sources, respectively (Fig. 3c, Supplementary Figs. 22 and 23). An isotope-labeled carbon dioxide ($^{13}CO_2$) photocatalytic reduction experiment based on LaNi-Phen/COF-5 is performed to investigate the origin of the CO_2RR products. As illustrated in Fig. 3d, the total ion chromatographic peak at ~ 7.45 min corresponds to CO, which generates three signals in the mass spectra (MS). The predominant MS signal at m/z = 29 corresponds to molecular ions of the ($^{13}CO^+$) peak of ^{13}CO, whilst the others ($^{13}C^+$ at m/z = 13 and O^+ at m/z = 16) originated from fragments of ^{13}CO, demonstrating that CO_2 gas is responsible for the formation of the carbon-related products. Cycling tests reveal that the CO_2RR evolution rate and selectivity exhibit only negligible losses after at least 5 cycles and a total irradiation time of 15 h, demonstrating that the LaNi-Phen/COF-5 catalyst possesses excellent structural robustness and durability in the CO_2RR (Fig. 3e). Furthermore, the heterogeneity tests demonstrate the heterogeneous nature of the LaNi-Phen/COF-5 catalysts (Supplementary Fig. 24 and Supplementary Note 5). Moreover, the XRD pattern, FTIR spectra, and XPS spectra of the recovered LaNi-Phen/COF-5 after 5 runs remain unchanged from the as-prepared sample (Supplementary Figs. 25–27). The catalyst's microstructure was retained during the CO_2RR process (Supplementary Figs. 28 and 29), demonstrating that La-Ni-Phen units are strongly maintained in the interior cavities of COF-5 colloid through the confinement effect of the pores. Photoelectrochemical measurements are performed to elucidate the separation and transfer capability of photogenerated carriers over LaNi-Phen/COF-5 (Supplementary Note 6). The steady-state photoluminescence (PL) emission intensity of LaNi-Phen/COF-5 is markedly more attenuated than that of pure COF-5 colloid, owing to improved exciton splitting and charge transfer (Supplementary Fig. 30)[43]. Noteworthy, when COF-5 colloid is only modified by La metal ions, a bathochromic shift ($\approx$ 26 nm) of the PL peak is observed, suggesting that the modulation of COF-5 colloid's optical properties can be attributed to La ions rather than Ni ions. Time-resolved photoluminescence (TR-PL) measurements illustrate that the carrier lifetimes of the photogenerated charges reduce from 4.75 ns (pure COF-5 colloid) to 0.53 ns (LaNi-Phen/COF-5), demonstrating that the lowering of the recombination of photogenerated charge carriers is due to the loading of COF-5 colloid with La and Ni ions (Supplementary Fig. 31 and Supplementary Table 6)[44]. Moreover, as evidenced by investigations of the transient photocurrent response and electrochemical impedance spectroscopy data, LaNi-Phen/COF-5 exhibits excellent charge separation efficiency of the photoinduced electron-hole pairs and low transfer resistance of the photogenerated charges (Supplementary Note 6 and Supplementary Figs. 32 and 33).

Reaction mechanism of CO $_2$ photoreduction to CO. The adsorbed CO probe molecule on various catalysts is analyzed using in-situ infrared spectroscopy to acquire a thorough understanding of the reaction mechanism of the CO_2 photoreduction. The bands in the range of 1800 to 1900 cm^{-1} correspond to the C-O stretching vibrations of bridging CO (CO_{bridge}) adsorbed on the La-Ni dual atom sites, and the intensity of CO absorption increases with irradiation time (Fig. 4a), whereas no obvious CO_{bridge} band is observed when using single La or Ni sites on COF-5 (Fig. 4b)[45,46]. These results illustrate unequivocally that only the construction of the La-Ni dual-atom catalyst provides efficient CO adsorption sites, enabling at the same time the synergistic effects discussed above as the source of the observed

outstanding photoelectric performance of the LaNi-Phen/COF-5 catalyst. In-situ XAFS measurements are performed to dynamically monitor the oxidation state of active sites to better understand their function on the atomic scale[47]. The Ni K-edge XANES spectra of LaNi-Phen/COF-5 clearly illustrate that the white-line intensity is slightly enhanced in a CO_2-saturated acetonitrile solution compared to that in an Ar-saturated acetonitrile solution, revealing the increase of the Ni oxidation state, which is generally ascribed to the spontaneous electron transfer from the active Ni center to the C 2p orbital of CO_2 during the adsorption and activation of CO_2. Interestingly, the white-line intensity of the Ni K-edge XANES spectra reduces slightly under the Xenon lamp irradiation and its position is between that of a CO_2-saturated and an Ar-saturated acetonitrile solution, demonstrating the gradual recovery of the active Ni center's oxidation state in the CO_2RR process. Furthermore, an oxidation state variation is observed in the La L3-edge XANES spectra (Supplementary Fig. 34). Summarizing, the in-situ XAFS analysis reveals that Ni atoms are the active centers for the CO_2RR, while La atoms are not only the optically active center but also the catalytically active center for CO_2 adsorption and activation.

The adsorbed surface species and CO_2-derived intermediates in the CO_2RR are dynamically monitored using in-situ diffuse reflectance infrared Fourier transform spectroscopy (DRIFTS). The time-resolved spectra of LaNi-Phen/COF-5 after introducing humid CO_2 in the dark display the characteristic infrared peaks of active $\cdot CO_2^-$ intermediates (v_s(O-C-O): 1634 cm^{-1}), bidentate carbonate (b-CO_3^{2-}, asymmetric CO_3 stretching vibration (v_{as}(CO_3): 1537−1562 cm^{-1}), monodentate carbonate (m-CO_3^{2-}, v_s(CO_3): 1494−1508 cm^{-1}), and bicarbonate HCO_3^- (σ(CHO): 1439−1462 cm^{-1}). Moreover, the CO_2 adsorption band (v_3(CO_2)) is indicated by a peak at approximately 3595−3727 cm^{-1}, and the intensities represent the CO_2 adsorption process in the LaNi-Phen/COF-5 catalysts (Fig. 4d and Supplementary Fig. 35)[48]. The subsequent CO_2RR on the surface of LaNi-Phen/COF-5 catalysts relies on an increased CO_2 adsorption capacity. As depicted in Fig. 4e, the generation of CO_2* at 1691 cm^{-1} with increasing light irradiation time implies activation of CO_2 through the route of $CO_2 + e^- \rightarrow CO_2$*, which is primarily ascribed to the facile transfer of the photogenerated electron to CO_2 molecules adsorbed on the LaNi-Phen/COF-5 surface[49]. Additionally, there is a significant increase in the intensities of the vibrational peaks at 1540 and 1511 cm^{-1}, assigned to the COOH* group[50]. During the CO_2RR process, the CO* absorption band at 2,036 cm^{-1} reveals the source of CO production in the photocatalytic system. Moreover, the CO_2RR process detects the formation of monodentate carbonate (m-CO_3^{2-}, v_s(CO_3): 1507 cm^{-1}) and bicarbonate HCO_3^- (σ(CHO): 1439 and 1701 cm^{-1})[51]. Based on these results, CO_2*, COOH*, and CO* species should be significant intermediates influencing the photoreduction performance of the LaNi-Phen/COF-5 catalysts. Furthermore, under light irradiation, these intermediates efficiently participate in the CO_2 conversion, which is accompanied by a gradual decrease in the intensities of the adsorbed CO_2 molecules (Supplementary Fig. 36).

Density functional theory (DFT) calculations are carried out to unveil the critical role of LaNi-Phen in the selective photoreduction of CO_2 to CO for further investigation of the CO_2RR process over LaNi-

Phen/COF-5. The CO_2 molecule bends after interacting with LaNi-Phen, as illustrated in Fig. 4f, demonstrating that C and O in activated CO_2* interact with the metallic Ni and La sites, respectively. The calculations demonstrate that the formation energy barrier of COOH* on LaNi-Phen/COF-5 is 0.74 eV, confirming that this process is the rate-limiting step. On the contrary, the formation energy barrier of the CO* intermediate is only 0.07 eV, implying that this process is thermodynamically favorable. Additionally, CO desorption is thermodynamically preferred over CHO* formation, with an energy barrier of 0.87 versus 1.14 eV, resulting in a promising photocatalytic performance with a high CO selectivity.

The HOMO-LUMO charge-transfer transitions of LaNi-Phen are also analyzed to further understand the role of atomic La in the CO_2RR enhancement mechanism (Fig. 4g). In particular, we demonstrate that the appropriate electronic characteristics of the La-Ni dual atomic sites in LaNi-Phen/COF-5 are responsible for providing the electrons for the CO_2 photoreduction. Among them, the HOMO energy level in LaNi-Phen is mainly located on Ni-Phen, whereas the LUMO level is on La-Phen, indicating that La-Phen in LaNi-Phen produces the necessary driving force for electron migration from the COF-5 colloid to the bimetallic La-Ni sites. The La atoms act as the optically active center and electron donor, continuously supplying photogenerated electrons to the LaNi-Phen/COF-5 system, while the COF-5 colloid acts as an electron bridge, directing to Ni atoms for the CO_2 photoreduction. Moreover, La-Phen exhibits an electrophilic LUMO level after transferring the photogenerated electron to the COF-5 colloid, leading to the spontaneous replenishment of the excess electrons in Ni-Phen back to La-Phen. This method regulates the product selectivity while enabling closed-loop utilization of the photoinduced charges. The aforementioned result is fully compatible with the proposed synergistic photocatalysis in LaNi-Phen/COF-5, which combines photoexcited charge-directed transfer with active CO_2 adsorption.

Combining the results of in-situ characterization and theoretical calculations allows us to corroborate the predicted CO_2RR mechanism of the LaNi-Phen/COF-5 diatomic photocatalyst (Fig. 4h), in which La atoms operate as optically active centers to promote the directional migration of photogenerated carriers and Ni atoms serve as functional catalytically active sites for the adsorption of activated CO_2. The design advantage of the novel system is the appropriate combination of light absorption and catalytic reaction processes on spatially close bimetallic centers supported on COF-5, which can efficiently overcome the longstanding problem of insufficient light absorption capacity for achieving high catalytic efficiency and CO-selectivity.

Discussion

We present a facile and scalable electrostatic self-assembly method to develop a COF-supported photocatalyst comprising La-Ni dual-atom active centers, in which La atoms serve as light-harvesting centers and Ni atoms provide high catalytic activity for the CO_2 photoreduction. The presented self-assembly process integrates both the La and Ni atoms into the COF-5 scaffold in single-site forms. The synergistic effect of the La-Ni double-atomic sites has been demonstrated using in-situ characterizations and theoretical calculations. Specifically, photoelectric characterizations revealed that they accelerate the

dynamic behavior of the photogenerated charge carriers, with Ni sites acting as the catalytic centers to promote CO_2 photoreduction through COOH* formation and CO***** dissociation and La sites favoring photogenerated electron transfer and long-lived charge separation. Therefore, LaNi-Phen/COF-5 exhibits a remarkable CO yield of 605.8 µmol g^{-1} h^{-1} and a high CO selectivity of 98.2% in the absence of any photosensitizer. This work highlights a novel approach for fabricating dual-atom photocatalysts with well-defined metallic centers inside porous COFs, in which the diatomic sites effectively combine light absorption and catalytic reaction cooperatively to achieve high CO_2RR performance. The straightforward preparation of the described photocatalyst paves the way for the development of related systems with tailored characteristics for the desired catalytic application.

Methods

Materials. $LaCl_3·6H_2O$ (99%), $NiCl_2·6H_2O$ (99%), and 1,10-Phenanthroline (Phen) were purchased from Aladdin. 2,3,6,7,10,11-Hexahydroxytriphenylene (HHTP) and 1,4-phenylenediboronic acid (PBBA) were provided by Jilin Chinese Academy of Sciences-Yanshen Technology Co., Ltd. as the precursors for COF-5 colloid. Acetonitrile (≥ 99.5%), mesitylene (98%) and 1,4-dioxane (≥ 99.5%) were supplied by Aladdin. 1,3-Dimethyl-2-phenyl-2,3-dihydro-1H-benzo[d]imidazole (BIH) was obtained from Bide Pharmatech Ltd. All reagents were of analytical grade and used without further purification.

Synthesis of the photocatalysts. *COF-5 colloid*. Colloidal COF-5 was synthesized by modifying the reported procedures[52,53]. Typically, HHTP (5 mM) and PBBA (7.5 mM) were dissolved in a mixture of acetonitrile: 1,4-dioxane: mesitylene (80:16:4 by volume; 20 mL) and sonicated for 3 min. The solution was subsequently filtered (0.45 µm PTFE) to remove insoluble particles. The solution was then heated to 90°C without stirring for 24 hours under atmospheric pressure. Finally, the resulting COF colloids were thoroughly washed three times with 10 mL acetone and resuspended with the aforementioned solvent mixture to obtain the final stable COF-5 colloidal suspension.

LaNi-Phen/COF-5. La and Ni ions were incorporated into the COF-5 colloid through adsorption and chelation with $LaCl_3·6H_2O$, $NiCl_2·6H_2O$, and 1,10-phenanthroline to synthesize LaNi-Phen/COF-5. The COF-5 colloid (3.3 mL, 10 mg) was dispersed in acetonitrile (5 mL) and stirred for half an hour to prepare the precursor solution. Afterward, $NiCl_2·6H_2O$ (0.52 mg, 2.2 µmol) was added to the aforementioned solution, which was then stirred for 30 min under an N_2 atmosphere. Then, Phen (18 mg, 0.1 mmol) was introduced to the precursor solution and stirred for 1 h to chelate Ni ions and prevent their aggregation. Finally, $LaCl_3·6H_2O$ (1.2 mg, 3.3 µmol) was added to the above-mentioned Ni-ion-containing solution and stirred for 12 h at 25°C under an N_2 atmosphere. LaNi-Phen/COF-5 precipitates were collected through centrifugation and then dried for 24 h at 60°C in a vacuum oven.

Ni-Phen/COF-5. Following a similar synthetic procedure to that of LaNi-Phen/COF-5, Ni-Phen/COF-5 catalyst was synthesized using 1.3 mg of $NiCl_2·6H_2O$ (5.5 µmol), without the addition of any other metal salts.

La-Phen/COF-5. Following a similar synthetic procedure to that of LaNi-Phen/COF-5, La-Phen/COF-5 was synthesized using 1.9 mg of $LaCl_3 \cdot 6H_2O$ (5.5 µmol).

Mix-LaNi-Phen/COF-5. The physical mixture of LaNi-Phen/COF-5 (labeled as Mix-LaNi-Phen/COF-5) was prepared by physically mixing 10 mg of La-Phen/COF-5 and 10 mg of Ni-Phen/COF-5.

Characterization. Powder X-ray diffraction (XRD) patterns of the samples were recorded on a desktop X-ray diffractometer (MiniFlex600/600-C) with Cu Kα radiation (λ = 1.5418 Å) in the range of 2θ from 2° to 40°. The morphology and microstructure of the samples were examined using High-resolution Transmission Electron Microscope (HRTEM, JEM-2100F, JEOL, Japan) and an Aberration-corrected high-angle annular dark-field scanning transmission electron microscopy (HAADF-STEM, Titan Cube Themis G2 300). The X-ray absorption structures at the Ni K-edge and La L3-edge of the LaNi-Phen/COF-5 were acquired in fluorescence excitation mode using a Lytle detector at the BL14W1-XAFS beamline of the Shanghai Synchrotron Radiation Facility (SSRF). The photon flux of the BL14W1-XAFS beamline is 5 × 10^{12} photons.s^{-1} at 10 keV, with a Si(111) DCM and a beam size of 100 × 200 µm^2. The k^3-weighted $\chi(k)$ data in k-space was Fourier-transformed to R space using Hanning windows in the Athena software to separate the EXAFS contributions from different coordination shells. The wavelet transform (WT) of EXAFS spectra was calculated using the Hama Fortran program. The XAFS fitting data was obtained using Artemis software to corroborate the local atomic structure and coordination environment of La and Ni atoms in the LaNi-Phen/COF-5 catalyst. The elemental composition of the samples was evaluated using an Energy Dispersive Spectrometer (EDS). X-ray photoelectron spectroscopy (XPS) measurements were performed on a Thermo ESCALAB 250 spectrometer. The position of the C 1s line at 284.8 eV was utilized to correct all XPS spectra. The Fourier transform infrared (FTIR) spectra of the samples were acquired using a Nicolet 6700 spectrometer. The Brunauer-Emmett-Teller (BET) surface area of the samples at 77 K was determined by N_2 adsorption and desorption isotherms using an ASAP 2460 system. The CO_2 adsorption capacity of the samples was also tested by ASAP 2460 system at 298 K. The diffuse reflectance spectra (DRS) of the samples were acquired using a UV-vis spectrophotometer (Shimadzu, UV-2550, Japan). The energy band structure of the samples was determined by measuring ultraviolet photoelectron spectra (UPS, ESCALAB 250Xi, Thermo Fisher Scientific, USA). The photo-generated charge carrier separation and lifetime of the samples were recorded using Steady-state Photoluminescence (PL) spectra (LabRam HR, HORIBA Jobin Yvon, France). Time-resolved photoluminescence (TRPL) spectra were recorded on a fluorescence lifetime spectrophotometer (Spirit 1040-8-SHG, Newport, US) at an excitation wavelength of 365 nm. Electrochemical impedance spectroscopy (EIS) and photocurrent measurements were performed on a CHI-660e workstation (Shanghai Chenhua Instruments Co.), with Pt wire, Ag/AgCl (saturated KCl), and 0.5 M Na_2SO_4 solution functioning as the counter electrode, reference electrode, and electrolyte, respectively.

Photocatalytic activities measurements. 10 mg of photocatalyst powder and 10 mM of BIH were mixed in a 50 mL solution containing 48 mL of acetonitrile and 2 mL of H_2O in a Pyrex glass reaction cell coupled to a CO_2 reduction system. After the airtight system was completely evacuated using a vacuum pump (no

O$_2$ or N$_2$ was detected by gas chromatography), ~ 80 kPa of high-purity CO$_2$ (99.999%) gas was injected. After the adsorption equilibrium, a 300 W xenon lamp (~ 100 mW/cm^2) was utilized as the light source to irradiate the photocatalytic cell, and the reaction system was kept at 10°C by cooling water. Gas chromatography (GC-2030, Shimadzu Corp., Japan) equipped with different chromatographic columns was employed to analyze produced H$_2$ and CO.

Isotope-labeling measurements. The carbon source for the isotope-labeling measurements was ^{13}CO$_2$ gas (Isotope purity, 99%, and chemical purity, 99.9%, Tokyo Gas Chemicals Co., Ltd.) instead of ^{12}CO$_2$ gas (Chemical purity, 99.999%, Showa Denko Gas Products Co., Ltd.). Typically, 10 mg of photocatalysts, 10 mM of BIH, 48 mL of acetonitrile, and 2 mL of water were loaded into the reaction cell. The ^{13}CO$_2$ photoreduction protocol was the same as described above, and the reduction products were further analyzed by gas chromatography-mass spectrometry (JMS-K9, JEOL-GCQMS, Japan and 6890N Network GC system, Agilent Technologies, USA) equipped with two different kinds of columns for detecting the products of ^{13}CO (HP-MOLESIEVE, 30 m × 0.32 mm × 25 µm, Agilent Technologies, USA).

In-situ diffuse reflectance infrared Fourier transform spectroscopy (DRIFTS) measurements. In-situ DRIFTS spectra were collected using an FT-IR spectrometer (Nicolet iS50 Thermo Scientific, USA) equipped with a mercury cadmium telluride (MCT) detector. Using an ultra-high vacuum pump to eliminate all of the gases in the reaction cell and adsorbed on the catalyst surface. The reaction cell was then filled with humid ultra-pure CO$_2$ gas (99.999%) or CO (99.999%) for CO$_2$ photoreduction or CO adsorption, respectively. Finally, the UV-vis light was turned on, and the in-situ DRIFTS data were collected using a difference value of 0 min in light to avoid signals from the organic ligand in the catalysts.

First-principles-based computational details. We have systematically calculated structural relaxation and electronic characteristics within the framework of Density Functional Theory (DFT) formalism as implemented in Materials Studio (MS). The general gradient approximation (GGA) in the form of a Perdew-Burke-Ernzerhof (PBE) exchange-correlation functional was employed for the self-consistent calculation. The energy cutoff utilized throughout the calculations was set at 700 eV, and the Brillouin zone was sampled using the 2×2×2 Monkhorst pack for the ionic relaxation of the system. The convergence thresholds for self-consistency and structural relaxation were set at 0.002 Hartree/Å for maximum force, 0.005 Å for maximum displacement, and 1.0×10^{-5} Hartree for energy change, respectively.

Declarations

Acknowledgements

Author contributions

Liu, Y.L., Peter, R., Chen, K.Q., Wang, S.Y., Chen, W., Ou, S.Y and Zhou, M. conceived and designed the experiments. Ou, S.Y. and Zhou, M carried out the synthesis of materials and photocatalytic test. Wang, Z.Q., performed the electronic structure calculations. Qi, K. and Ma, J.Y. performed the XENAS test. Ou, S.Y., Zhou, M., Mei, A.H., Yang, Z.F. was involved in material test characterization and data analysis. Liu, Y.L., Peter, R., Chen, K.Q. and Wang, S.Y., supervised the project. Liu, Y.L., Peter, R., Chen, K.Q., Wang, S.Y., Ou, S.Y and Zhou, M. wrote the paper. All authors discussed the results and commented on the manuscript.

Competing interests

The authors declare no competing financial interest.

References

1. Niu, K. *et al.* A spongy nickel-organic CO_2 reduction photocatalyst for nearly 100% selective CO production. Sci. Adv. **3**, e1700921 (2017).
2. Dong, L. *et al.* Stable heterometallic cluster-based organic framework catalysts for artificial photosynthesis. Angew. Chem. Int. Ed. **59**, 2659–2663 (2020).
3. Zeng, S. *et al.* Optical control of selectivity of high rate CO_2 photoreduction via interband- or hot electron Z-scheme reaction pathways in Au-TiO_2 plasmonic photonic crystal photocatalyst. Appl. Catal. B-Environ. **267**, 118664 (2020).
4. Studt, F. *et al.* Discovery of a Ni-Ga catalyst for carbon dioxide reduction to methanol. Nat. Chem. **6**, 320–324 (2014).
5. Fu, J. W. *et al.* Graphitic carbon nitride with dopant induced charge localization for enhanced photoreduction of CO_2 to CH_4. Adv. Sci. **6**, 1900796 (2019).
6. Wang, S. L. *et al.* Porous hypercrosslinked polymer-TiO_2-graphene composite photocatalysts for visible-light-driven CO_2 conversion. Nat. Commun. **10**, 676 (2019).

7. Zhao, Y. F. *et al.* Two-dimensional-related catalytic materials for solar-driven conversion of CO_x into valuable chemical feedstocks. Chem. Soc. Rev. **48**, 1972–2010 (2019).

8. Diercks, C. S., Liu, Y. Z., Cordova, K. E. & Yaghi, O. M. The role of reticular chemistry in the design of CO_2 reduction catalysts. Nat. Mater. **17**, 301–307 (2018).

9. Ran, J. R., Jaroniec, M. & Qiao, S. Z. Cocatalysts in semiconductor-based photocatalytic CO_2 reduction: achievements, challenges, and opportunities. Adv. Mater. **30**, 1704649 (2018).

10. Chen, P. *et al.* Rare-earth single-atom La-N charge-transfer bridge on carbon nitride for highly efficient and selective photocatalytic CO_2 reduction. ACS Nano **14**, 15841–15852 (2020).

11. Wang, Z. Y. *et al.* Room-temperature synthesis of single iron site by electrofiltration for photoreduction of CO_2 into tunable syngas. ACS Nano **14**, 6164–6172 (2020).

12. Sharma, P. *et al.* Carbon nitride-based ruthenium single atom photocatalyst for CO_2 reduction to methanol. Small **17**, 2006478 (2021).

13. Di, J. *et al.* Isolated single atom cobalt in Bi_3O_4Br atomic layers to trigger efficient CO_2 photoreduction. Nat. Commun. **10**, 2840 (2019).

14. Jiang, Z. Y. *et al.* Living atomically dispersed Cu ultrathin TiO_2 nanosheet CO_2 reduction photocatalyst. Adv. Sci. **6**, 1900289 (2019).

15. Lee, B. H. *et al.* Reversible and cooperative photoactivation of single-atom Cu/TiO_2 photocatalysts. Nat. Mater. **18**, 620–626 (2019).

16. Xue, Z. H., Luan, D. Y., Zhang, H. B. & Lou X. W. Single-atom catalysts for photocatalytic energy conversion. Joule **6**, 92–133 (2022).

17. Gao, C., Low, J. X., Long, R., Kong, T. T., Zhu, J. F. & Xiong, Y. J. Heterogeneous single-atom photocatalysts: Fundamentals and applications. Chem. Rev. **120**, 12175–12216 (2020).

18. Zhang, H. B. *et al.* Efficient visible-light-driven carbon dioxide reduction by a single-atom implanted metal-organic framework. Angew. Chem. Int. Ed. **55**, 14308–14312 (2016).

19. Hannagan, R. T., Giannakakis, G., Flytzani-Stephanopoulos, M. & Sykes, E. C. H. Single-atom alloy catalysis. Chem. Rev. **120**, 12044–12088 (2020).

20. Han, L. L. *et al.* Stable and efficient single-atom Zn catalyst for CO_2 reduction to CH_4. J. Am. Chem. Soc. **142**, 12563–12567 (2020).

21. Gao, G. P., Jiao, Y., Waclawik, E. R. & Du, A. J. Single atom (Pd/Pt) supported on graphitic carbon nitride as an efficient photocatalyst for visible-light reduction of carbon dioxide. J. Am. Chem. Soc. **138**, 6292–6297 (2016).

22. Bai, L. C., Hsu, C. S., Alexander, D. T. L., Chen, H. M. & Hu, X. L. A cobalt-iron double-atom catalyst for the oxygen evolution reaction. J. Am. Chem. Soc. **141**, 14190–14199 (2019).

23. Feng, W. H. *et al.* Insights into bimetallic oxide synergy during carbon dioxide hydrogenation to methanol and dimethyl ether over $GaZrO_x$ oxide catalysts. ACS Catal. **11**, 4704–4711 (2021).

24. Ying, Y. R., Luo, X., Qiao, J. L. & Huang, H. T. "More is different:" synergistic effect and structural engineering in double-atom catalysts. Adv. Funct. Mater. **31**, 2007423 (2021).

25. Li, H. L. *et al*. Synergetic interaction between neighbouring platinum monomers in CO_2 hydrogenation. Nat. Nanotechnol. **13**, 411–417 (2018).

26. Cheng, L. *et al*. Dual-single-atom tailoring with bifunctional integration for high-performance CO_2 photoreduction. Adv. Mater. **33**, 2105135 (2021).

27. Li, J. *et al*. Self-adaptive dual-metal-site pairs in metal-organic frameworks for selective CO_2 photoreduction to CH_4. Nat. Catal. **4**, 719–729 (2021).

28. An, B. *et al*. Cooperative copper centres in a metal-organic framework for selective conversion of CO_2 to ethanol. Nat. Catal. **2**, 709–717 (2019).

29. Lin, L. *et al*. Synergistic catalysis over iron-nitrogen sites anchored with cobalt phthalocyanine for efficient CO_2 electroreduction. Adv. Mater. **31**, 1903470 (2019).

30. Ren, W. H. *et al*. Isolated diatomic Ni-Fe metal-nitrogen sites for synergistic electroreduction of CO_2. Angew. Chem. Int. Ed. **58**, 6972–6976 (2019).

31. Li, X. D. *et al*. Selective visible-light-driven photocatalytic CO_2 reduction to CH_4 mediated by atomically thin $CuIn_5S_8$ layers. Nat. Energy **4**, 690–699 (2019).

32. Lu, M. *et al*. Installing earth-abundant metal active centers to covalent organic frameworks for efficient heterogeneous photocatalytic CO_2 reduction. Appl. Catal. B-Environ. **254**, 624–633 (2019).

33. Liu, W. B. *et al*. A scalable general synthetic approach toward ultrathin imine-linked two-dimensional covalent organic framework nanosheets for photocatalytic CO_2 reduction. J. Am. Chem. Soc. **141**, 17431–17440 (2019).

34. Zhong, W. F. *et al*. A covalent organic framework bearing single Ni sites as a synergistic photocatalyst for selective photoreduction of CO_2 to CO. J. Am. Chem. Soc. **141**, 7615–7621 (2019).

35. Yang, S. Z. *et al*. 2D covalent organic frameworks as intrinsic photocatalysts for visible light-driven CO_2 reduction. J. Am. Chem. Soc. **140**, 14614–14618 (2018).

36. Lu, M. *et al*. Rational design of crystalline covalent organic frameworks for efficient CO_2 photoreduction with H_2O. *Angew*. Chem. Int. Ed. **58**, 12392–12397 (2019).

37. Lei, K. *et al*. A metal-free donor-acceptor covalent organic framework photocatalyst for visible-light-driven reduction of CO_2 with H_2O. Chemsuschem **13**, 1725–1729 (2020).

38. Fu, Y. H., Zhu, X. L., Huang, L., Zhang, X. C., Zhang, F. M. & Zhu, W. D. Azine-based covalent organic frameworks as metal-free visible light photocatalysts for CO_2 reduction with H_2O. Appl. Catal. B-Environ. **239**, 46–51 (2018).

39. Sun, W. W. *et al*. Coordination-induced interlinked covalent- and metal-organic-framework hybrids for enhanced lithium storage. Adv. Mater. **31**, 1903176 (2019).

40. Lu, M. *et al*. Confining and highly dispersing single polyoxometalate clusters in covalent organic frameworks by covalent linkages for CO_2 photoreduction. J. Am. Chem. Soc. **144**, 1861–1871

(2022).

41. Wang, H. *et al.* Covalent organic framework photocatalysts: Structures and applications. Chem. Soc. Rev. **49**, 4135–4165 (2020).

42. Cote, A. P., Benin, A. I., Ockwig, N. W., O'Keeffe, M., Matzger, A. J. & Yaghi, O. M. Porous, crystalline, covalent organic frameworks. Science **310**, 1166–1170 (2005).

43. Gong, Y. N. *et al.* Regulating photocatalysis by spin-state manipulation of cobalt in covalent organic frameworks. J. Am. Chem. Soc. **142**, 16723–16731 (2020).

44. Xia, Y. *et al.* Highly selective CO_2 capture and its direct photochemical conversion on ordered 2D/1D heterojunctions. Joule **3**, 2792–2805 (2019).

45. Papasizza, M. & Cuesta, A. In situ monitoring using ATR-SEIRAS of the electrocatalytic reduction of CO_2 on Au in an ionic liquid/water mixture. ACS Catal. **8**, 6345–6352 (2018).

46. Perez-Martinez, L., de los Toyos, L. M. M., Shibuya, J. J. T. & Cuesta, A. Methanol dehydrogenation on Pt electrodes: active sites and role of adsorbed spectators revealed through time-resolved ATR-SEIRAS. ACS Catal. **11**, 13483–13495 (2021).

47. Ji, S. F. *et al.* Rare-earth single erbium atoms for enhanced photocatalytic CO_2 reduction. Angew. Chem. Int. Ed. **59**, 10651–10657 (2020).

48. Sheng, J. P. *et al.* Identification of halogen-associated active sites on bismuth-based perovskite quantum dots for efficient and selective CO_2-to-CO photoreduction. ACS Nano **14**, 13103–13114 (2020).

49. Wu, J. *et al.* Efficient visible-light-driven CO_2 reduction mediated by defect-engineered BiOBr atomic layers. Angew. Chem. Int. Ed. **57**, 8719–8723 (2018).

50. Yang, P. J., Wang, R. R., Tao, H. L., Zhang, Y. F., Titirici, M. M. & Wang, X. C. Cobalt nitride anchored on nitrogen-rich carbons for efficient carbon dioxide reduction with visible light. Appl. Catal. B-Environ. **280**, 119454 (2021).

51. Liu, Y. P., Shen, D. Y., Zhang, Q., Lin, Y. & Peng, F. Enhanced photocatalytic CO_2 reduction in H_2O vapor by atomically thin Bi_2WO_6 nanosheets with hydrophobic and nonpolar surface. Appl. Catal. B-Environ. **283**, 119630 (2021).

52. Smith, B. J. *et al.* Colloidal covalent organic frameworks. ACS Central Sci. **3**, 58–65 (2017).

53. Flanders, N. C. *et al.* Large exciton diffusion coefficients in two-dimensional covalent organic frameworks with different domain sizes revealed by ultrafast exciton dynamics. J. Am. Chem. Soc. **142**, 14957–14965 (2020).
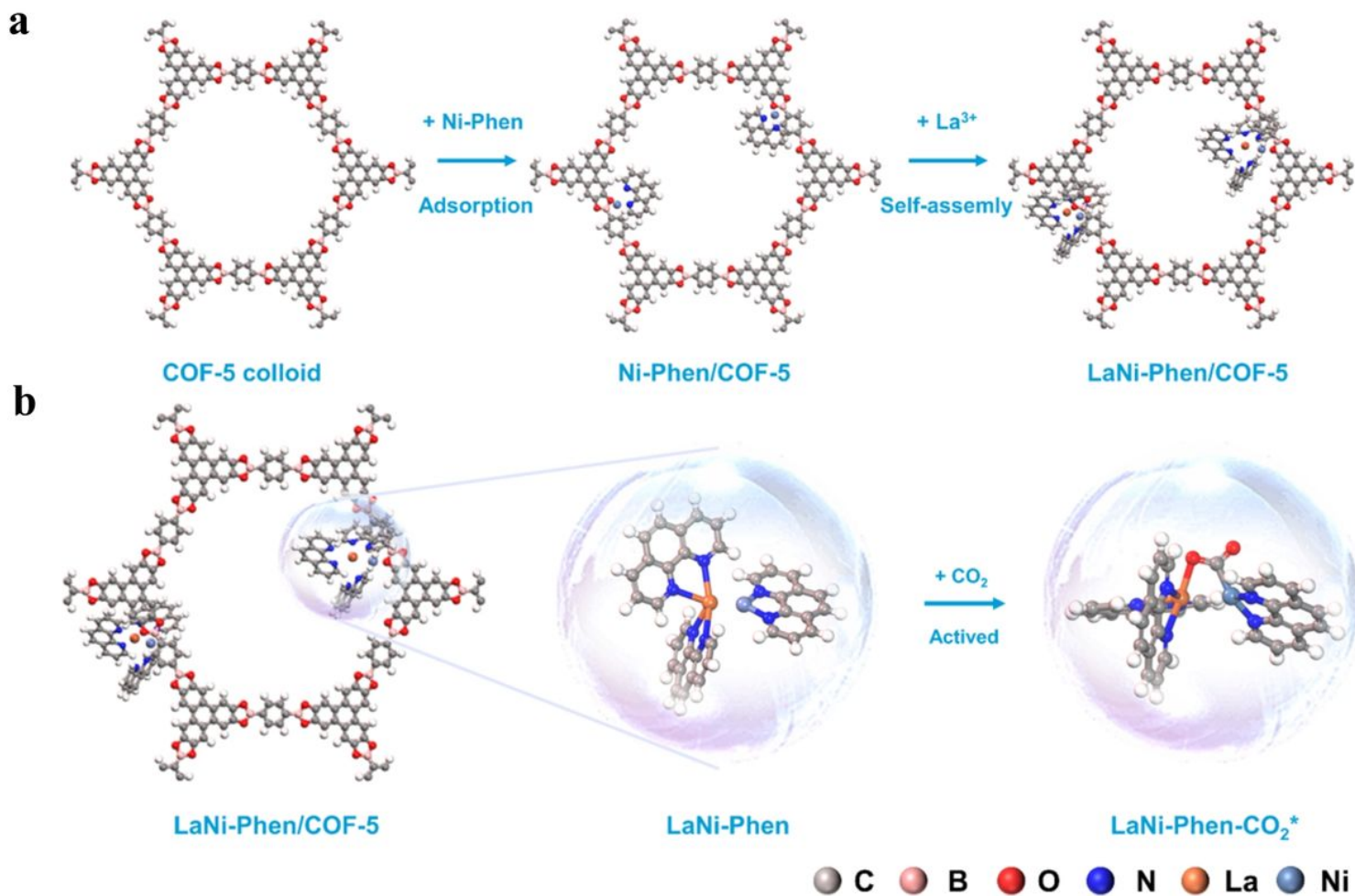
Figures

Figure 1

Schematic illustration of the construction of the diatomic sites and CO$_2$RR. (a) Self-assembly of LaNi-Phen into COF-5 colloid to create the diatomic site photocatalyst. **(b)** Schematic diagram of photocatalytic CO$_2$ reduction in LaNi-Phen/COF-5. Color code: carbon-grey, oxygen-red, boron-pink, hydrogen-white, nitrogen-blue, nickel-light blue, lanthanum-orange. The same color scheme is applied in Fig. 2 and 4.
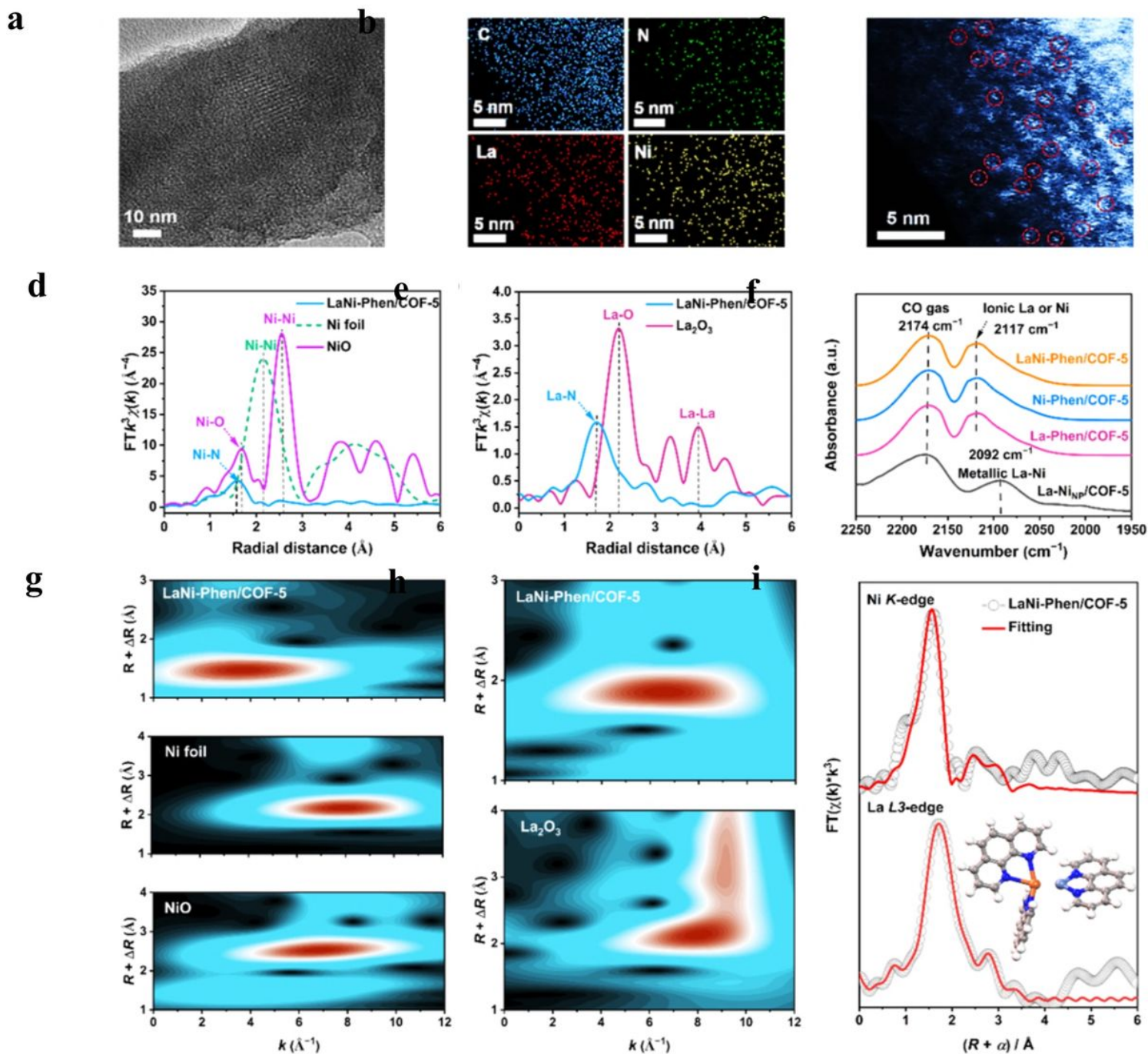
Figure 2

Visualization and spectroscopic characterization of LaNi-Phen/COF-5. **(a)** HR-TEM image, **(b)** energy-dispersive spectroscopy mapping, **(c)** atomic-resolution HAADF-STEM images of LaNi-Phen/COF-5. **(d)** Ni K-edge Fourier transformed EXAFS spectra, **(e)** La L3-edge Fourier transformed EXAFS spectra. **(f)** DRIFTS spectra of adsorbed CO on La-Phen/COF-5, Ni-Phen/COF-5, LaNi-Phen/COF-5, and a reference material comprising metallic La and Ni. **(g)** Wavelet transform (WT) of the LaNi-Phen/COF-5, NiO, and Ni foil samples, **(h)** WT of LaNi-Phen/COF-5, and La_2O_3 samples. **(i)** Ni K-edge and La L3-edge EXAFS (points) and curve-fit (line) for LaNi-Phen/COF-5, shown in R-space. The data are k^3-weighted and not phase-corrected.
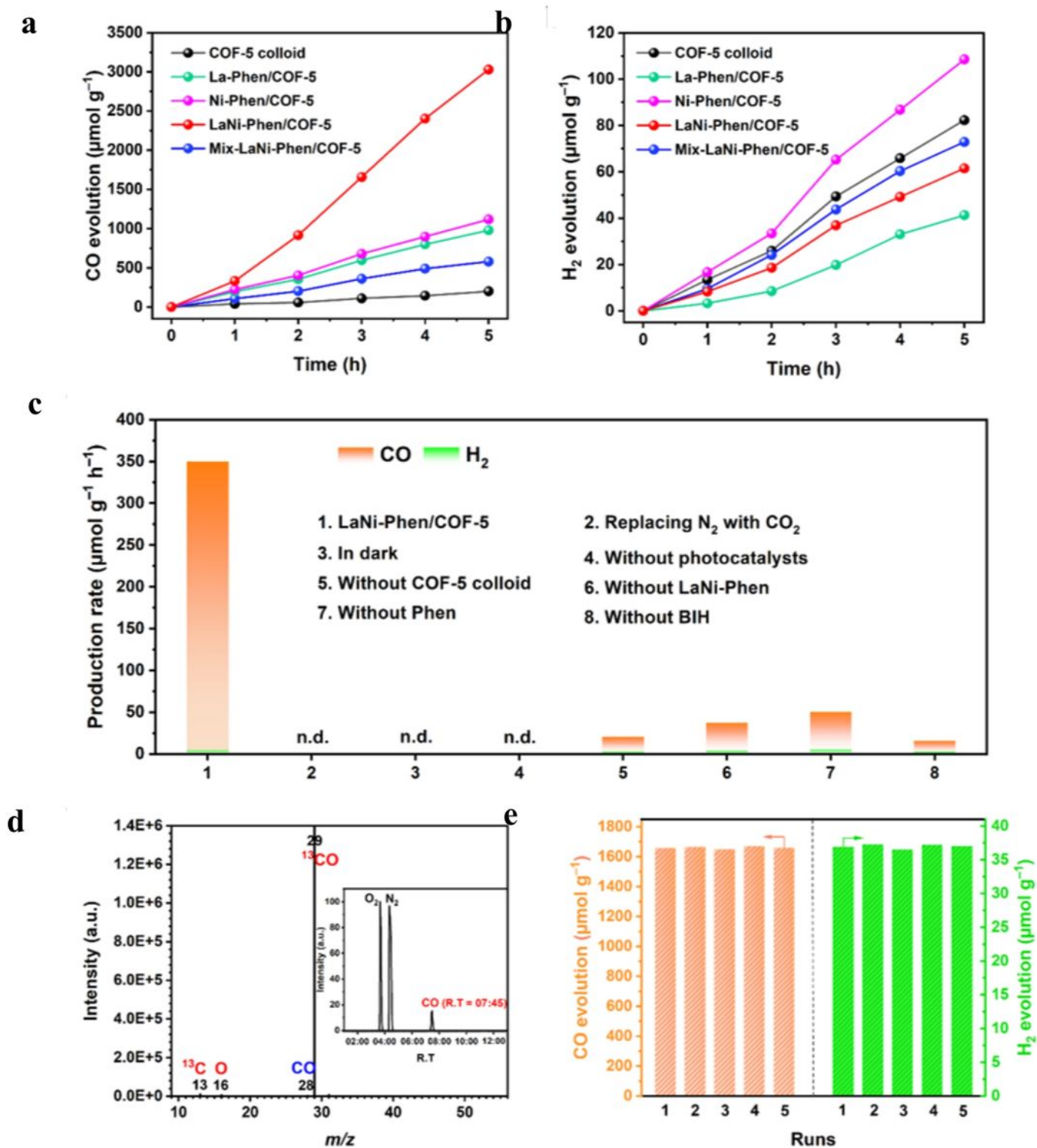
Figure 3

Photocatalytic CO₂ reduction performance. (a-b) Time-dependent CO **(a)** and H₂ **(b)** evolution curves under UV-Vis light irradiation ($\lambda > 380$ nm) within 5 h using COF-5 colloid (black spheres), La-Phen/COF-5 (green spheres), Ni-Phen/COF-5 (pink spheres) LaNi-Phen/COF-5 (red spheres) and mix-LaNi-Phen/COF-5 (blue spheres). **(c)** Control experiments of the photocatalytic CO₂ reduction performance over LaNi-Phen/COF-5 under altered conditions. **(d)** Mass spectra of ^{13}CO (m/z = 29) produced and total ion

chromatography (inset) in the photocatalytic reduction of $^{13}CO_2$ over LaNi-Phen/COF-5. **(e)** CO and H_2 production rates in cycling experiments over LaNi-Phen/COF-5.
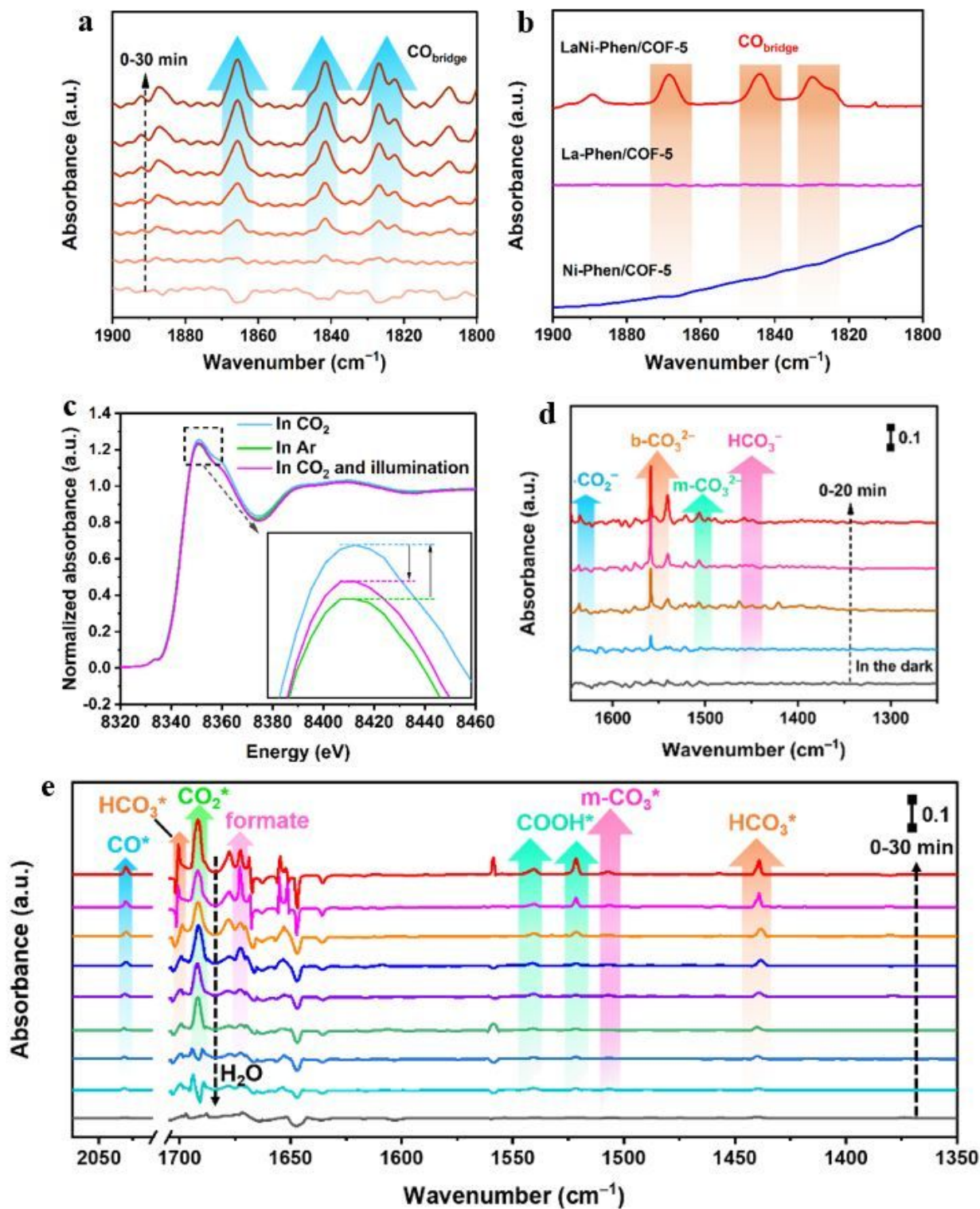

Figure 4

Detection of the reaction mechanism for the photoreduction of CO_2 to CO. (a) In-situ DRIFTS spectra of adsorbed CO at 1800-1900 cm^{-1} for detecting the effective active site over LaNi-Phen/COF-5. **(b)** DRIFTS

spectra of adsorbed CO at 1800-1900 cm^{-1} over La-Phen/COF-5, Ni-Phen/COF-5, and LaNi-Phen/COF-5. (c) Ni K-edge XANES spectra of LaNi-Phen/COF-5 in CO_2 photoreduction reduction reaction at room temperature and 1 atm of Ar or CO_2-saturated aqueous solution (inset: the enlarged Ni K-edge XANES spectra). (d) In-situ DRIFTS spectra of CO_2 and H_2O interaction with LaNi-Phen/COF-5 in the dark. (e) In-situ DRIFTS spectra at 1350-2070 cm^{-1} for detecting the reaction intermediates in CO_2 photoreduction and recording the adsorption and activation of CO_2 over LaNi-Phen/COF-5 in the presence of H_2O under subsequently light irradiation.
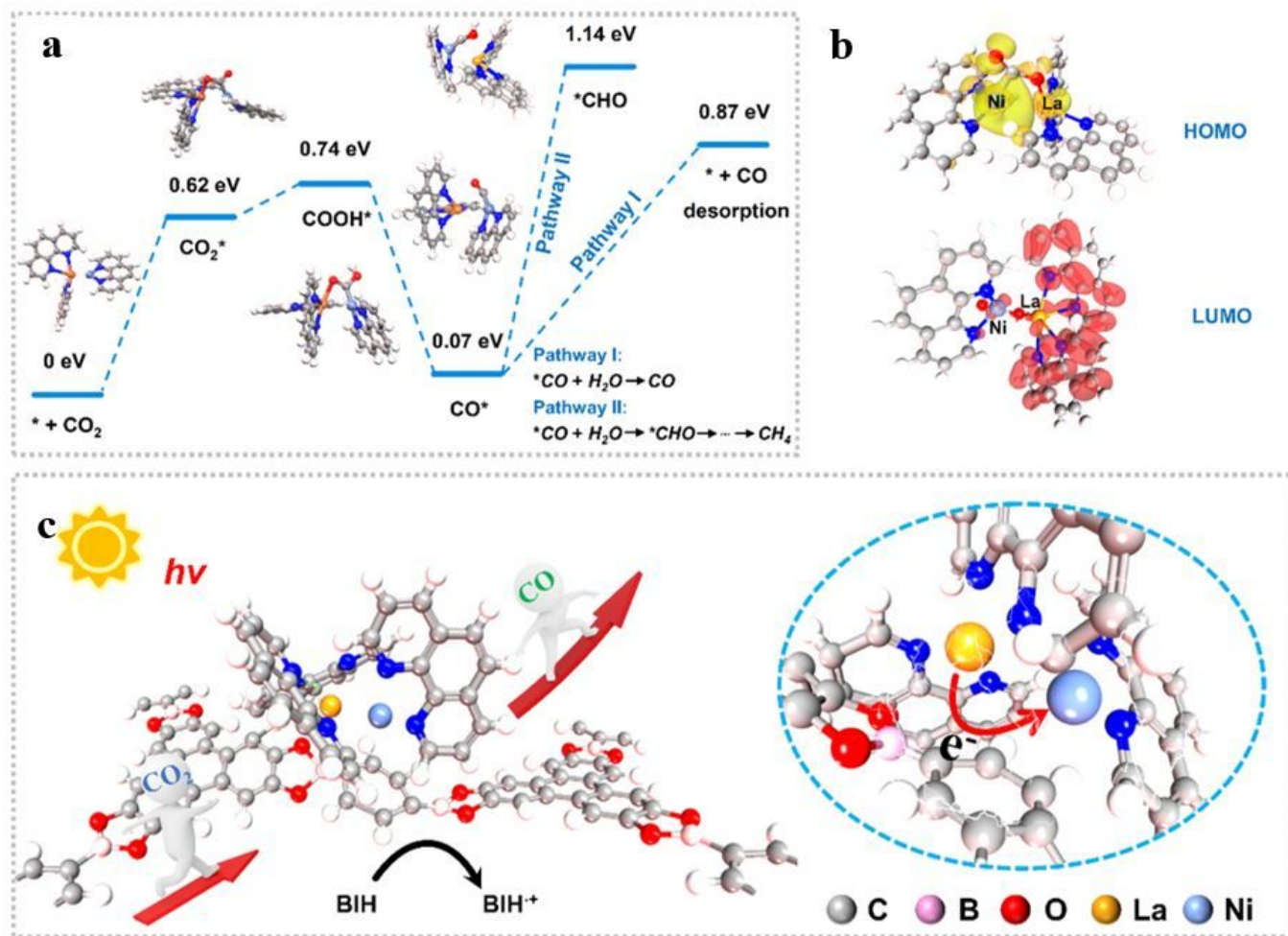

Figure 5

Analysis of the reaction mechanism for the photoreduction of CO_2 to CO

(a) Reaction pathways for CO_2 photoreduction on LaNi-Phen/COF-5 with corresponding geometry structures. (b) HOMO-LUMO charge-transfer transitions for LaNi-Phen. (c) Schematic illustration of charge transfer in the photocatalytic CO_2 reaction over LaNi-Phen/COF-5.

Supplementary Files

This is a list of supplementary files associated with this preprint. Click to download.

- SupplementaryInformation.docx
- TOC.jpg
- Associatedcontent.docx